Understanding Energy Efficiency and Interference Tolerance in Millimeter Wave Receivers

Panagiotis Skrimponis*, Seongjoon Kang*, Abbas Khalili*, Wonho Lee†, Navid Hosseinzadeh†,
Marco Mezzavilla*, Elza Erkip*, Mark J. W. Rodwell†, James F. Buckwalter†, Sundeep Rangan*
*NYU Tandon School of Engineering, New York University, Brooklyn, NY
†Dept. ECE, University of California, Santa Barbara

Abstract—**Power consumption is a key challenge in millimeter wave (mmWave) receiver front-ends, due to the need to support high dimensional antenna arrays at wide bandwidths. Recently, there has been considerable work in developing low-power front-ends, often based on low-resolution ADCs and low-power mixers. A critical but less studied consequence of such designs is the relatively low-dynamic range which in turn exposes the receiver to adjacent carrier interference and blockers. This paper provides a general mathematical framework for analyzing the performance of mmWave front-ends in the presence of out-of-band interference. The goal is to elucidate the fundamental trade-off of power consumption, interference tolerance and in-band performance. The analysis is combined with detailed network simulations in cellular systems with multiple carriers, as well as detailed circuit simulations of key components at $140\,\mathrm{GHz}$. The analysis reveals critical bottlenecks for low-power interference robustness and suggests designs enhancements for use in practical systems.**

I. INTRODUCTION

A key challenge in millimeter wave (mmWave) receiver front-ends is power consumption, particularly for mobile and portable devices. High power consumption is especially challenging in emerging systems above $100\,\mathrm{GHz}$ that need to support a large number of array elements at high bandwidths with relatively poor device efficiency [1]–[6].

Significant recent progress has been made with reduced power architectures, most notably via low-resolution analog-to-digital converters (ADCs) and phase shifters, as well low-power mixers [7]–[13]. A common theme in these designs is to sacrifice dynamic range for lower power. This design choice is often based on the fact that communication systems in the mmWave bands typically operate at relatively low signal-to-noise ratios (SNRs) per antenna that can be recovered from beamforming.

However, most prior analyses of low-dynamic range architectures have generally only considered the *in-band* signal distortion. Aggressive use of low dynamic range front-ends introduces potential susceptibility of the receiver to high power *out-of-band* or adjacent carrier signals [14]–[16]. These
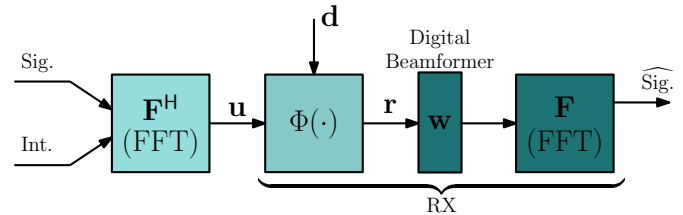
Fig. 1. Abstract mathematical model for a system with adjacent carrier interference and non-linear, noisy front-end. Sig. and Int. denote the desired signal and interference signal from the other transmitters, respectively.

adjacent carrier signals can be particularly large in uncoordinated cellular deployments with multiple carriers as well as unlicensed use [17].

For receiver design in conventional bands below $6\,\mathrm{GHz}$, it is well-known that interference rejection (also called *blockers*) can be the dominant driver of power consumption. Some example low-power designs with good out-of-band blocker performance can be found in [18]–[20]. However, the design and analysis of low power designs under adjacent carrier interference in the mmWave range face unique challenges. Most importantly, standard SAW and BAW (surface acoustic wave and bulk acoustic wave) filters are not easily available in these frequencies [21]. Recent work has attempted to use filters integrated into the package [22]–[24], but these come with added RF signal loss. In addition, the nonlinearities inherent in low-power mmWave designs can be difficult to analyze and mitigate against. For example, there has been some recent work studying jamming signals on mmWave receivers with low-resolution ADCs and other non-linear hardware impairments in [14], [16], [25], [26]. However, these works generally consider the case where the jamming signal is in-band, but spatially separated from the desired signal. In this work, we focus on adjacent carrier interference where interfering signal is in a different frequency band, as would occur in cellular, licensed deployments.

For mmWave systems under adjacent carrier interference, we thus wish to understand the fundamental relation between power consumption and interference tolerance and how this trade-off can be best optimized. Towards this end, the contributions of the paper are three-fold: First, building on the work in [3], [4], [27], [28], we provide a general methodology

for mathematically analyzing the sensitivity of receivers from adjacent carrier emissions. Importantly, the framework can incorporate general power spectral densities of the interfering signals, models of the filters at various points in the receiver chain, as well as non-linearity and quantization limits in the analog front-end.

Secondly, we apply the methodology to practical designs of 28 GHz and 140 GHz receivers. The analysis uses detailed circuit and signal processing simulations to provide realistic estimates on the power consumption and elucidate the main bottlenecks in interference rejection robustness.

Finally, we perform simple network simulations at 28 GHz and 140 GHz to estimate the frequency of high-power adjacent carrier signals in likely cellular deployments with multiple carriers. The simulations consider cases with non-co-located cell sites, which introduce the highest level of interference [17].

II. SYSTEM MODEL

The model is an extension of the analysis framework in [3], [4], [27], [28], which studied a single transmitter and receiver. Here, we extend the model to add interfering transmitters. The basic set-up is shown in Fig. 1.

As in [3], [4], [27], [28], we model the transmissions in discrete-time frequency-domain and assume there are N frequency bins. We divide the bins into two groups:

- $I_{\text{sig}} \subseteq \{1, \ldots, N\}$ representing the frequency bins on which the desired signal is transmitted; and
- $I_{\text{int}} = \{1, \ldots, N\} \backslash I_{\text{sig}}$ representing the frequency bins on which the interference appears.

We assume that each transmitter performs digital beamforming and has only one output stream. We denote the frequency domain symbols for the desired signal by s_n, $n \in I_{\text{sig}}$ and the interfering signal samples by v_n, $n \in I_{\text{int}}$. As a result, the input to the channel is the signal,

$$\mathbf{u} = \mathbf{F}^{\mathsf{H}}\mathbf{x}, \quad x_n = \begin{cases} s_n & \text{if } n \in I_{\text{sig}} \\ v_n & \text{if } n \in I_{\text{int}} \end{cases}, \quad (1)$$

where $\mathbf{F}^{\mathsf{H}} \in \mathbb{C}^{n \times n}$ is the unitary IFFT matrix converting the frequency-domain vector to time-domain. As for the power levels, we assume that the transmitted symbols, s_n, are zero-mean complex Gaussian with energy per transmitted sample of $E_{\text{sig}} = \mathbb{E}|s_n|^2$ and the interference symbols are also complex Gaussian with a frequency-dependent energy per sample, $E_{\text{int}} = \mathbb{E}|v_n|^2$. We will assume there is some reference thermal noise level N_0 and let

$$\gamma_{\text{sig}} := \frac{E_{\text{sig}}}{N_0}, \quad \gamma_{\text{int}} := \frac{E_{\text{int}}}{N_0},$$

denote the signal and interference-to-noise ratios.

The samples u_n are passed through a generic channel and receiver radio frequency front-end (RFFE) which are jointly modeled as a non-linear, memoryless function $\Phi(u_n, \mathbf{d}_n)$, where $\mathbf{d}_n$ are i.i.d. noise vectors with i.i.d. elements that include thermal noise and noise from the non-linear components.
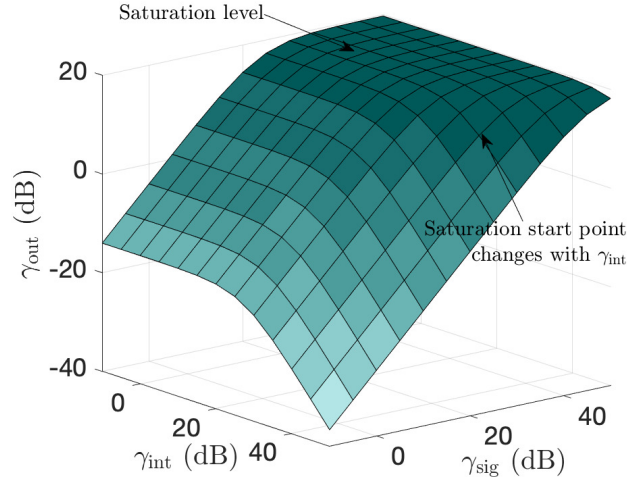

Fig. 2. Input-output SNR relation.

Finally, the receiver performs digital beamforming using the vector $\mathbf{w}$

$$r_n = \mathbf{w}^{\mathsf{H}}\Phi(u_n, \mathbf{d}_n). \quad (2)$$

III. CAPACITY BOUND AND OUTPUT SNR

Our goal is to characterize the performance of the discussed model in Sec. II in terms of the spectral efficiency. To this end, similar to [3], we make use of the concepts of the output SNR and input-output SNR relation described next.

From Sec. II, we have

$$\hat{\mathbf{x}} = \mathbf{F}\Phi(\mathbf{F}^{\mathsf{H}}\mathbf{x}, \mathbf{D}). \quad (3)$$

Assuming that the variables $\hat{x}_n$, $\mathbf{d}_n$, and x_n have an underlying statistical model and are distributed as $\hat{X}$, D, and X, respectively, we can use the Bussgang-Rowe decomposition [29], [30] and model the non-linearity in the system (i.e., $\Phi(\cdot)$) as multiplying a scalar with its input and adding a noise which is uncorrelated with the input. More precisely, we can write

$$\hat{X} = AX + T, \quad \mathbb{E}|T|^2 = \tau, \quad (4)$$

where

$$A := \frac{\mathbb{E}\left[\hat{X}^*X\right]}{\mathbb{E}|X|^2}, \quad \tau := \mathbb{E}|\hat{X} - AX|^2, \quad (5)$$

with X^* denoting the complex conjugate of X.

In general, both A and τ are functions of the input SNR γ_{in} so we may write $A = A(\gamma_{\text{in}})$ and $\tau = \tau(\gamma_{\text{in}})$. From (4), we can then define the *output SNR* off the desired signal $\mathbf{s}$ as,

$$\gamma_{\text{out}} = G(\gamma_{\text{in}}) := \frac{|A(\gamma_{\text{in}})|^2}{\tau(\gamma_{\text{in}})}\gamma_{\text{sig}}. \quad (6)$$

This is the SNR that would be seen in attempting to recover the input transmitted vector $\mathbf{s}$ from the output vector $\hat{\mathbf{s}}$.
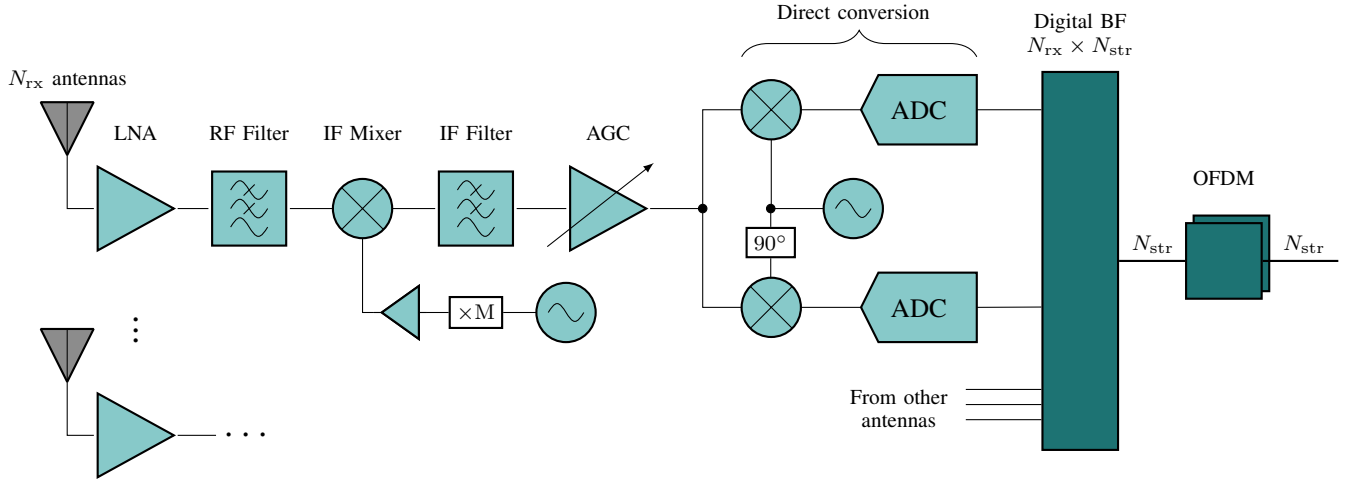
646

Fig. 3. High-level architecture of a fully-digital superheterodyne receiver architecture. The architecture supports N_{rx} antennas and N_{str} digital streams. The light green boxes represent analog and the dark-green boxes the digital components. In the RF front-end, some component are not shown.

<table>
<tr><td colspan="5" align="center">TABLE I
PARAMETERS OF THE 28 GHz RFFE DEVICES USED IN THE ANALYSIS.</td></tr>
</table>

Parameter	LNA$^{(1)}$	LNA$^{(2)}$	Mixer$^{(1)}$	Mixer$^{(2)}$
Design [μm]	10	5	2	5
Noise Figure [dB]	2.13	2.53	9.039	7.542
Gain [dB]	14.26	12.85	0.16	3.558
IIP3 [dBm]	-1.456	0.603	-3.1	2.1
Power [mW]	8.91	5.34	4.838	7.03

<table>
<tr><td colspan="5" align="center">TABLE II
PARAMETERS OF THE 140 GHz RFFE DEVICES USED IN THE ANALYSIS.</td></tr>
</table>

Parameter	LNA$^{(1)}$	LNA$^{(2)}$	Mixer$^{(1)}$	Mixer$^{(2)}$
Design [μm]	4	2-4	1	1
Noise Figure [dB]	7.50	7.48	21.53	20.47
Gain [dB]	11.13	16.56	-1.74	-0.52
IIP3 [dBm]	-9.15	-8.90	-4.45	-3.88
Power [mW]	4.80	15.90	5.00	5.00

Using the SNR enables us to bound the performance of the system in terms of the capacity. More precisely, using same steps as of [3, Appendix A], we can show that the capacity of the system can is lower bounded as,

$$C \geq \frac{N_{\text{sig}}}{N} f_s \log_2 \left(1 + \gamma_{\text{out}}\right), \qquad (7)$$

where f_s is the sample rate and $N_{\text{sig}} = |I_{\text{sig}}|$ represent the number of frequency bins for the signal. Moreover, assuming that the ADC performs oversampling with the ratio ζ, using same steps as of [3, Appendix B], we have

$$C \geq \frac{N_{\text{sig}}\zeta}{N} f_s \log_2 \left(1 + \frac{\gamma_{\text{out}}}{\zeta}\right), \qquad (8)$$

In this paper, we will show through detailed simulations that the input-output SNR relation can be approximated in the form of

$$\hat{\gamma}_{\text{out}} = \frac{\beta\gamma_{\text{sig}}}{1 + \alpha_1\gamma_{\text{sig}} + \alpha_2\gamma_{\text{int}}}, \qquad (9)$$

where $\gamma_{\text{int}} = \frac{1}{|I_{\text{int}}|}\sum_{n \in I_{\text{int}}} E_i[n]$. for three parameters β and α_1 and α_2 using which we can evaluate the receiver front-end performance. Intuitively, this formula suggest that due to the non-linearity in the system: (i) the signal energy is reduced; (ii) a ratio of the signal is distorted; (iii) a ratio of the adjacent band signal (i.e., interference) is leaked to the desired band.

From (9), we also observe that the output SNR saturates to the value of $\frac{\beta}{\alpha_1}$ as the input signal SNR increases. Furthermore, for higher values of the interference signal the saturation should accrue for lower values of the input SNR. One can also observe these from Fig. 2 which illustrates (9) for a fixed values of β, α_1 and α_2 and different values of desired and interference signal powers.

IV. LINK-LAYER SIMULATION

The model in Section II is a simplified abstraction of an actual RFFE. In this section, we validate the model and extract the parameters for (9) with realistic, circuit simulations of potential RFFEs at 28 GHz and 140 GHz.

A. Signal and interference model

We consider a downlink scenario in a communication link between an NR basestation (gNB) and a mobile device (UE). For each slot, the gNB generates a physical downlink shared channel (PDSCH) that includes both information and control signals. The receiver uses the demodulation reference signal (DM-RS) for practical channel estimation. To compensate the common phase error (CPE) the 3GPP 5G NR, standard introduce the phase tracking reference signal (PT-RS). The receiver performs coherent CPE estimation using the algorithm described in [31]. For time synchronization, between the gNB and UE we utilize the primary (PSS) and the secondary synchronization signals (SSS).
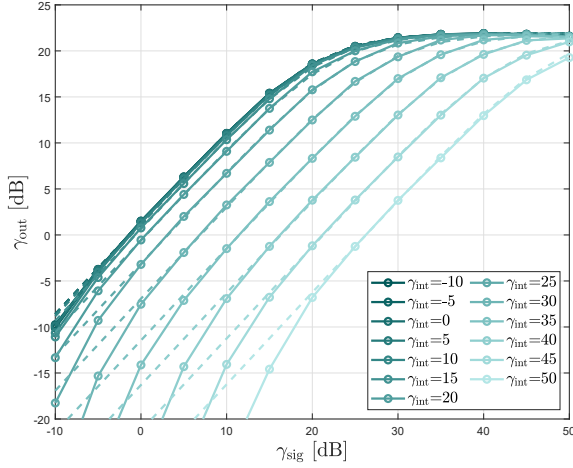
647

Fig. 4. Evaluation of the approximation model in (9) for Design[1] at 28 GHz for different input interference power.

Parameter	28 GHz		140 GHz	
	Design[1]	Design[2]	Design[1]	Design[2]
β	1.3865	1.2725	0.3099	0.1862
α_1	0.0090	0.0024	0.0021	0.0004
α_2	0.0058	0.0017	0.0014	0.0003
RX antennas	16	16	64	64
NF [dB]	2.78	3.08	9.40	11.50
Power [mW]	411	404	1682	1355

power dividers and amplifiers. They provide a method to determine the best configuration of LO drivers that achieve the same performance for a minimum power.

Using the components and the optimization framework described in [28] we select two of the optimized designs for the 140 GHz systems in our analysis. These two designs achieve similar performance to the state-of-the-art design discussed in [4] while achieving a significant improvement in power consumption. Similarly, for the 28 GHz devices we design two common base emitter base collector (CBEBC) LNAs, and two active mixers based on the common Gilbert cell design. We use the optimization framework in [28] to determine the number of LO drivers. For both frequencies, Design[1] use 4-bit ADCs while Design[2] use 5-bit ADC pairs. This assumption is based on prior works [8]–[10], [32] indicating that 4 bits are sufficient for the majority of cellular data and control operations. Based on a flash-based 4-bit ADC in [33], we consider the ADC FOM = 65 fJ/conv. We summarize the parameters for the devices at 28 GHz and 140 GHz in Table I and Table II respectively.

C. Model fitting

For each receiver design we fit a model in form of (9). Since this nonlinear function $\Phi(\cdot)$ depends on the parameters α_1, α_2, and β we can write the estimated output-SNR model as $\hat{\gamma}_{\text{out}}(\gamma_{\text{sig}}, \gamma_{\text{int}}; \alpha_1, \alpha_2, \beta)$. For the *initial heuristic* fit we set,

$$\beta = \frac{1}{F}, \quad \alpha_1 = \alpha_2 = \frac{1}{\gamma_{\text{sat}}F}, \quad (10)$$

where F is the noise factor of the system, and γ_{sat} the saturation SNR in linear scale. We then optimize the fit using the non-linear least squares regression method and optimize a problem of the following form,

$$Q(\gamma_{\text{sig}}, \gamma_{\text{int}}) := \min_{\alpha_1, \alpha_2, \beta} \|\gamma_{\text{out}}(\gamma_{\text{sig}}, \gamma_{\text{int}}) - \hat{\gamma}_{\text{out}}(\gamma_{\text{sig}}, \gamma_{\text{int}}; \alpha_1, \alpha_2, \beta))\|_2^2, \quad (11)$$

where γ_{out} are the measurements from the link-layer simulation using (6), and $\hat{\gamma}_{\text{out}}$ is the estimate using the model in (9). The optimized parameters for the 140 GHz and 28 GHz receiver designs are summarized in Tab. III. In Fig. 4 we show that the model in (9) provides a very good fit. In particular, we see the linear regime for low-input SNR and the saturation for high-input signal power. We show that as the input interference increases the model the saturation SNR is also changing.

To model the interference, we assume the presence of another gNB that generates i.i.d. $\mathcal{CN}(0,1)$ symbols in frequency-domain. The symbols are modulated with OFDM to generate interference in an adjacent band. Even though the signals from the two gNBs are originally independent in the frequency domain, the presence of the non-linear processing introduces distortion to the main signal from the adjacent band. As explained in Section II, this increase the total received energy and causes the RFFE saturation point to happen much earlier.

B. Receiver configurations

Similarly to [28] we consider a fully-digital superheterodyne receiver architecture as shown in Fig. 3. The receiver has $N_{\text{rx}} = 16$ or 64 antennas with independent RFFE processing. The received signal is amplified with a low-noise amplifier (LNA), downconverted with an intermediate frequency (IF) mixer, amplified with an automated gain control (AGC) amplifier before the direct conversion mixer, and finally quantized with a pair of ADCs. The system use filters in the RF and IF domain to improve the image rejection and the dynamic range of the system. The actions of the RFFE devices for each receiver configuration is modeled with a different non-linear function $\Phi(\cdot)$.

In [28] the authors design and evaluate RFFE devices at 140 GHZ based on a 90 nm SiGE BiCMOS HBT technology. They focus on minimizing the power consumption of the RFFE devices at a certain performance in terms of gain, noise figure (NF), and the input third order intercept point (IIP3). The LNA designs vary in terms of number of stages, topology, and transistor size. While the proposed double-balanced active mixers are all based on the conventional Gilbert-cell design, they vary in transistor size. The mixer performance characteristics depend on the input power from the local oscillator (LO). To further optimize the power consumption of the receiver, the authors propose a novel LO distribution model. Specifically, the mixers in the same tile share a common LO driver using

648

Fig. 5. Signal and interfering paths in a system with two carriers.

Parameter	Value	
Carrier frequency, [GHz]	28	140
Total bandwidth, [MHz]	190.80	380.16
Sample rate, [MHz]	491.52	1966.08
gNB antenna configuration	8×8	16×16
UE antenna configuration	4×4	8×8
Area [m^2]	1000×1000	
UE and gNB min. distance [m]	10	
ISD [m]	200	
gNB height [m]	$\mathcal{U}(2,5)$	
UE height [m]	1.6	
gNB TX power [dBm]	30	
gNB downtilt angle	$-12°$	
gNB number of sectors	3	
Vertical half-power beamwidth	$65°$	
Horizontal half-power beamwidth	$65°$	

V. NETWORK-LEVEL SIMULATION

The above analysis shows that the performance of the RFFE degrades in the presence of strong out-of-band interference when the front-end dynamic range is low. This fact raises a basic question: *how often is the adjacent carrier interference strong in practical systems?* In this section, we perform a simple network simulation to assess the effect of adjacent carrier interference in a downlink cellular system with two adjacent carriers, carriers A and B.

We take account of a wrap-around $1\,\mathrm{km} \times 1\,\mathrm{km}$ network area to conduct the network-level simulation. Subject to a inter-site distance (ISD), gNBs are deployed by homogeneous Poisson point process (HPPP) with density $\lambda = \frac{4}{\pi \times \mathrm{ISD}^2}$, and accordingly, the same number of UEs are uniformly distributed. Furthermore, all gNBs and UEs are randomly assigned to carrier A or B. We use the notation gNB$_A$ and gNB$_B$ for base stations, and UE$_A$ and UE$_B$ for UEs. Individual gNBs are multi-sectorized with 8×8 uniform rectangular arrays (URA) per sector which is tilted down by $-12°$, while each UE is equiped with a URA. The full parameter settings are shown in Table IV.

Fig. 5 shows the scenario for analyzing the interference between adjacent carrier frequencies. A UE in carrier A will receive the desired signal from its serving BS and interference signal from non-serving BSs in carrier A in the same carrier and from all BSs in carrier B.

For every gNB-UE pair, we generate a multi-path channel for two different frequency cases, $28\,\mathrm{GHz}$ and $140\,\mathrm{GHz}$, according to [34] and compute the SNR for downlink case. Specifically, we employ the path-loss model specified in [34] for the Urban Micro Street Canyon (Umi-Street-Canyon) environment. The 3GPP NR standard is very flexible and we assume the channel models described in [34] will hold for the $140\,\mathrm{GHz}$ communication systems.

Within each carrier, we then assume that each UE is served by the strongest gNB. As a simplification, the gNBs and UEs then beamform along the strongest path with no regard to interference nulling to other UEs. A sufficient number of UEs are dropped such that we can obtain one UE served by each sector in each gNB. Hence, the simulation drop represents one point in time where each gNB is using its entire bandwidth on one UE.

With the channels and beamforming direction, we can then estimate the effective SINR at each UE. Following the model (9), we estimate the SINR as:

$$\gamma = \frac{\beta E_{\mathrm{sig}}^a}{E_{\mathrm{kT}} + \alpha_1 E_{\mathrm{tot}}^a + \alpha_2 E_{\mathrm{tot}}^b}. \tag{12}$$

Here, E_{sig}^a and E_{int}^a is the energy per sample of the serving and interfering signals including the beamforming and element gains at the TX and RX, and E_{kT} is the thermal noise. The distortion from the non-linearities is modeled by two terms: $\alpha_1 E_{\mathrm{tot}}^a$ captures the distortion from the total power from all base stations in carrier A (serving and non-serving); $\alpha_2 E_{\mathrm{tot}}^b$ captures the distortion from the total power from all base stations in the adjacent carrier, carrier B. For these terms, we assume that the distortion is spatially white so we do not add the RX beamforming gains on each path. The terms however do include the TX element and beamforming gains as well as the RX element gain.

Fig. 6 shows the SNR distributions for the designs discussed in Section IV at $28\,\mathrm{GHz}$ and $140\,\mathrm{GHz}$. As a performance benchmark, we compare the SNR distribution under three models:

- SNR with adjacent carrier interference and in-band distortion: This is the model (12) with the parameters for α_1 and α_2 in Table III found from the circuit simulations. The resulting SNR CDF is shown in the dashed line in Fig. 6.
- SNR with no adjacent carrier interference and in-band distortion: This is the model (12) with the parameters for α_1 in Table III but $\alpha_2 = 0$. The SNR CDF is shown in the dotted line in Fig. 6.
- SNR with no adjacent carrier interference and no in-band distortion: This is the model (12) with the parameters for $\alpha_1 = \alpha_2 = 0$. The resulting SNR CDF is shown in the solid line in Fig. 6.
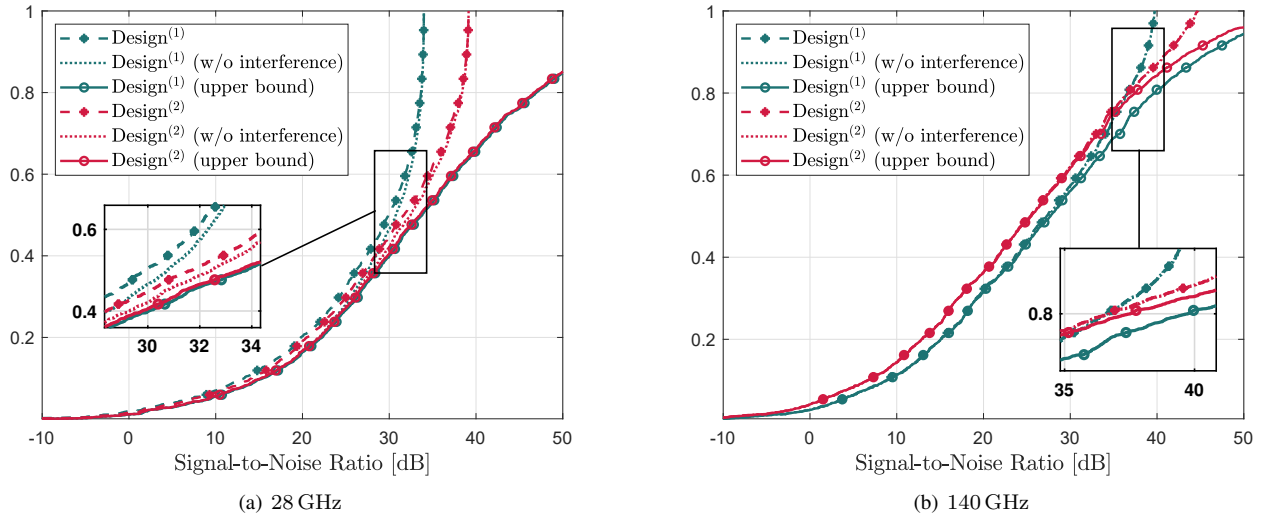
649

(a) 28 GHz

(b) 140 GHz

Fig. 6. Estimated distribution of downlink SNRs with different carrier frequencies and different RFFE designs. The plots show the SNR under the full model (12) with distortion from adjacent carrier interference and in-band signal; the SNR with no adjacent carrier interference distortion ($\alpha_2 = 0$); and the SNR with no in-band or adjacent carrier interference distortion ($\alpha_1 = \alpha_2 = 0$).

Comparing the plots, we observe that the impact of distortion from adjacent carrier interference is negligible. This suggests that for these parameters, there may be no need for extra filtering in the RF/IF or baseband to suppress the adjacent carrier interference. Thus, we can conclude that by optimizing the RFFE devices and reducing the dynamic range of the system, we can improve the energy efficiency without being vulnerable from the adjacent carrier interference. Furthermore, as expected the designs at 28 GHz have lower saturation points comparing to the 140 GHz designs, due to the difference in the beamforming gain resulted from the difference in the number of antennas.

As explained in Section IV, at 140 GHz we expect the designs to have different performance. In the low-SNR regime Design$^{(1)}$ performs better due to the lower NF, while Design$^{(2)}$ performs better in the high-SNR regime due to the larger number of ADC bits.

VI. CONCLUSIONS

Low-power designs for receivers above 100 GHz have traditionally relied on operating the circuits with limited dynamic range either via low-resolution ADCs or low-power mixers. While there techniques have been successful when considering in-band signal distortion, the limited dynamic range can be an issue for adjacent carrier interference. We have developed a simple mathematically model to describe this effect and fit the model parameters on realistic circuit designs at 28 GHz and 140 GHz. The models were then be used in a simple network simulation to estimate the effect of adjacent carrier interfence in cellular systems with two operators. Our preliminary simulations suggest that, at least under the parameters considered, highly optimized power designs are not significantly vulnerable to adjacent carrier interference. Future work can consider other deployments

where the adjacent carrier interference could be higher. For example, short range local area signals operating adjacent to cellular bands as well as mixed applications such as terrestrial networks sharing spectrum with vehicular or UAV systems.

REFERENCES

[1] R. Méndez-Rial, C. Rusu, A. Alkhateeb, N. González-Prelcic, and R. W. Heath, "Channel estimation and hybrid combining for mmWave: Phase shifters or switches?" in *2015 Information Theory and Applications Workshop (ITA)*. IEEE, 2015, pp. 90–97.

[2] T. S. Rappaport, Y. Xing, O. Kanhere, S. Ju, A. Madanayake, S. Mandal, A. Alkhateeb, and G. C. Trichopoulos, "Wireless communications and applications above 100 GHz: Opportunities and challenges for 6G and beyond," *IEEE Access*, vol. 7, pp. 78 729–78 757, 2019.

[3] P. Skrimponis, S. H. Mirfarshbafan, C. Studer, and S. Rangan, "Power efficient multi-carrier baseband processing for 5G and 6G wireless," in *2020 54th Asilomar Conference on Signals, Systems, and Computers*, 2020, pp. 324–330.

[4] P. Skrimponis, S. Dutta, M. Mezzavilla, S. Rangan, S. H. Mirfarshbafan, C. Studer, J. Buckwalter, and M. Rodwell, "Power consumption analysis for mobile mmWave and sub-THz receivers," in *2020 2nd 6G Wireless Summit (6G SUMMIT)*, 2020, pp. 1–5.

[5] L. Yan, C. Han, and J. Yuan, "A dynamic array-of-subarrays architecture and hybrid precoding algorithms for terahertz wireless communications," *IEEE Journal on Selected Areas in Communications*, vol. 38, no. 9, pp. 2041–2056, 2020.

[6] J. Tan and L. Dai, "THz precoding for 6G: Applications, challenges, solutions, and opportunities," *arXiv preprint arXiv:2005.10752*, 2020.

[7] A. H. Naqvi and S. Lim, "Review of recent phased arrays for millimeter-wave wireless communication," *Sensors*, vol. 18, no. 10, p. 3194, 2018.

[8] W. B. Abbas, F. Gomez-Cuba, and M. Zorzi, "Millimeter wave receiver efficiency: A comprehensive comparison of beamforming schemes with low resolution ADCs," *IEEE Transactions on Wireless Communications*, vol. 16, no. 12, pp. 8131–8146, 2017.

[9] J. Zhang, L. Dai, X. Li, Y. Liu, and L. Hanzo, "On low-resolution ADCs in practical 5G millimeter-wave massive MIMO systems," *IEEE Communications Magazine*, vol. 56, no. 7, pp. 205–211, 2018.

[10] M. Abdelghany, A. A. Farid, U. Madhow, and M. J. Rodwell, "Towards all-digital mmWave massive MIMO: Designing around nonlinearities," in *Proc. IEEE Asilomar Conference on Signals, Systems, and Computers*, 2018, pp. 1552–1557.

[11] H. Yan and D. Cabric, "DSP linearization for millimeter-wave all-digital receiver array with low-resolution ADCs," in *2019 IEEE 20th International Workshop on Signal Processing Advances in Wireless Communications (SPAWC)*, 2019, pp. 1–5.

[12] J. Mo, A. Alkhateeb, S. Abu-Surra, and R. W. Heath, "Hybrid architectures with few-bit ADC receivers: Achievable rates and energy-rate tradeoffs," *IEEE Transactions on Wireless Communications*, vol. 16, no. 4, pp. 2274–2287, 2017.

[13] S. Jacobsson, G. Durisi, M. Coldrey, U. Gustavsson, and C. Studer, "Throughput analysis of massive MIMO uplink with low-resolution ADCs," *IEEE Transactions on Wireless Communications*, vol. 16, no. 6, pp. 4038–4051, 2017.

[14] G. Marti, O. Castañeda, S. Jacobsson, G. Durisi, T. Goldstein, and C. Studer, "Hybrid jammer mitigation for all-digital mmwave massive MU-MIMO," 2021.

[15] G. Marti, O. Castañeda, and C. Studer, "Jammer mitigation via beam-slicing for low-resolution mmwave massive MU-MIMO," *IEEE Open Journal of Circuits and Systems*, vol. 2, p. 820–832, 2021.

[16] H. Akhlaghpasand, E. Björnson, and S. M. Razavizadeh, "Jamming-robust uplink transmission for spatially correlated massive MIMO systems," *CoRR*, vol. abs/2002.12581, 2020.

[17] M. Rebato, F. Boccardi, M. Mezzavilla, S. Rangan, and M. Zorzi, "Hybrid spectrum sharing in mmWave cellular networks," *IEEE Transactions on Cognitive Communications and Networking*, vol. 3, no. 2, pp. 155–168, 2017.

[18] P. Sepidband and K. Entesari, "A CMOS wideband receiver resilient to out-of-band blockers using blocker detection and rejection," *IEEE Transactions on Microwave Theory and Techniques*, vol. 66, no. 5, pp. 2340–2355, 2018.

[19] K. Trotskovsky, A. Whitcombe, G. Lacaille, A. Puglielli, P. Lu, Z. Wang, N. Narevsky, G. Wright, A. M. Niknejad, B. Nikolić *et al.*, "A 0.25–1.7-GHz, 3.9–13.7-mW power-scalable,- 10-dBm harmonic blocker-tolerant mixer-first RF-to-digital receiver for massive MIMO applications," *IEEE Solid-State Circuits Letters*, vol. 1, no. 2, pp. 38–41, 2018.

[20] A. Agrawal and A. Natarajan, "An interferer-tolerant CMOS code-domain receiver based on N-path filters," *IEEE Journal of Solid-State Circuits*, vol. 53, no. 5, pp. 1387–1397, 2018.

[21] S. Mahon, "The 5G effect on RF filter technologies," *IEEE Transactions on Semiconductor Manufacturing*, vol. 30, no. 4, pp. 494–499, 2017.

[22] A. O. Watanabe, M. Ali, S. Y. B. Sayeed, R. R. Tummala, and P. M. Raj, "A review of 5G front-end systems package integration," *IEEE Transactions on Components, Packaging and Manufacturing Technology*, 2020.

[23] Z. Siddiqui, M. Sonkki, K. Rasilainen, J. Chen, M. Berg, M. E. Leinonen, and A. Pärssinen, "Dual-Polarized Filtering Antenna for mm-Wave 5G Base Station Antenna Array," in *2021 15th European Conference on Antennas and Propagation (EuCAP)*. IEEE, 2021, pp. 1–4.

[24] X. Gu, D. Liu, Y. Hasegawa, K. Masuko, C. Baks, Y. Suto, Y. Fujisaku, B. Sadhu, A. Paidimarri, N. Guan *et al.*, "Antenna-in-Package Integration for a Wideband Scalable 5G Millimeter-Wave Phased-Array Module," *IEEE Microwave and Wireless Components Letters*, vol. 31, no. 6, pp. 682–684, 2021.

[25] H. Pirzadeh, G. Seco-Granados, and A. L. Swindlehurst, "Mitigation of jamming attack in massive MIMO with one-bit FBB sigma-delta ADCs," in *2019 53rd Asilomar Conference on Signals, Systems, and Computers*. IEEE, 2019, pp. 1700–1704.

[26] S. Jacobsson, U. Gustavsson, G. Durisi, and C. Studer, "Massive MU-MIMO-OFDM uplink with hardware impairments: Modeling and analysis," *CoRR*, vol. abs/1812.02078, 2018.

[27] S. Dutta, A. Khalili, E. Erkip, and S. Rangan, "Capacity bounds for communication systems with quantization and spectral constraints," in *2020 IEEE International Symposium on Information Theory (ISIT)*, 2020, pp. 2038–2043.

[28] P. Skrimponis, N. Hosseinzadeh, A. Khalili, E. Erkip, M. J. W. Rodwell, J. F. Buckwalter, and S. Rangan, "Towards energy efficient mobile wireless receivers above 100 GHz," *IEEE Access*, vol. 9, pp. 20 704–20 716, 2021.

[29] J. J. Bussgang, "Crosscorrelation functions of amplitude-distorted gaussian signals," 1952.

[30] H. Rowe, "Memoryless nonlinearities with gaussian inputs: Elementary results," *The BELL system technical Journal*, vol. 61, no. 7, pp. 1519–1525, 1982.

[31] V. Syrjala, M. Valkama, N. N. Tchamov, and J. Rinne, "Phase noise modelling and mitigation techniques in OFDM communications systems," in *2009 Wireless Telecommunications Symposium*, 2009, pp. 1–7.

[32] S. Dutta, C. N. Barati, D. Ramirez, A. Dhananjay, J. F. Buckwalter, and S. Rangan, "A case for digital beamforming at mmWave," *IEEE Transactions on Wireless Communications*, pp. 1–1, 2019.

[33] B. Nasri, S. P. Sebastian, K. D. You, R. RanjithKumar, and D. Shahrjerdi, "A 700 uW 1GS/s 4-bit folding-flash ADC in 65nm CMOS for wideband wireless communications," in *Proc. ISCAS*, May 2017, pp. 1–4.

[34] 3GPP, "TR 38.901, 3rd Generation Partnership Project; Technical Specification Group Radio Access Network; Study on channel model for frequencies from 0.5 to 100 GHz ," 2019.